Research Square

Preprints are preliminary reports that have not undergone peer review.
They should not be considered conclusive, used to inform clinical practice,
or referenced by the media as validated information.

# Graphene-Tunable Broadband Reflective Metasurface for Terahertz Polarization Conversion and Refractive-Index Biosensing

**Harish Raizada**[1]

harish.ec.22@nitj.ac.in

Dr. B. R. Ambedkar National Institute of Technology

**Nitesh Kashyap**[2]

Dr. B. R. Ambedkar National Institute of Technology

**Research Article**

**Keywords:** Terahertz Metasurface, Biosensor, Fractional Bandwidth, Polarization Conversion Ratio, Refractive Index

**Posted Date:** November 23rd, 2026

**DOI:** https://doi.org/10.21203/rs.3.rs-11716506/v1

**License:** This work is licensed under a Creative Commons Attribution 4.0 International License.
Read Full License

**Additional Declarations:** No competing interests reported.

# Graphene-Tunable Broadband Reflective Metasurface for Terahertz Polarization Conversion and Refractive-Index Biosensing

**Harish Raizada[1]*, Nitesh Kashyap[2]**

[1]Department of Electronics and Communication Engineering, Dr. B. R. Ambedkar National Institute of Technology, Jalandhar 144008, Punjab, India.
[2]Department of Electronics and Communication Engineering, Dr. B. R. Ambedkar National Institute of Technology, Jalandhar 144008, Punjab, India.

*Corresponding Author
E-mail:harish.ec.22@nitj.ac.in

## Abstract

Broadband operation, high conversion efficiency, electrical tunability, and sensing functionality are often challenges that must be met simultaneously in refractive-index sensors and terahertz polarization converters. We propose a small graphene-based reflective metasurface for refractive-index sensing and multifunctional terahertz polarization conversion. The proposed structure includes a polyimide dielectric spacer, an aluminum ground plane, asymmetric aluminum resonating elements, and a graphene layer that provides an electrically tunable electromagnetic response. The designed structural asymmetry and strong resonant coupling enable effective dual-band broadband polarization conversion, with a polarization conversion ratio (PCR) over 90% across two frequency bands, 6.108–10.773 THz and 11.648–14.051 THz. This results in a total bandwidth of 7.068 THz with an average PCR of 95.98%. In addition, three sub-bands with a total bandwidth of 3.736 THz, an average PCR of 98.31%, and a maximum conversion efficiency of almost 99.95% are used to realize a PCR above 96%. Furthermore, the polarization-conversion response is studied at oblique incidence up to 45°, showing large resonance shifts and PCR degradation for angles above approximately 20°, but good spectrum retention at low-to-moderate incidence angles. We demonstrate the tunability enabled by graphene by varying the chemical potential from 0.1 to 1.0 eV, resulting in tunable spectral changes with excellent conversion efficiency. The systematic shift of the PCR cutoff frequencies for sensing applications, due to a change in refractive index from 1.00 to 1.40, yields maximum sensitivities of 2.2234 THz/RIU at the higher cutoff frequency and 3.5772 THz/RIU at the lower cutoff frequency ( local maxima between n =1.00 and 1.05; the linear -fit sensitivities over n =1.00-1.40 are 1.177THz/RIU and 1.454 THz/RIU , respectively).. Therefore, the proposed small platform is suitable for multifunctional terahertz applications, including broadband polarization conversion, electrical tunability, and high-sensitivity refractive-index sensing.

**Keywords:** Terahertz Metasurface, Biosensor, Fractional Bandwidth, Polarization Conversion Ratio, Refractive Index

## 1. Introduction

Metasurfaces are two-dimensional surfaces with subwavelength-scale structures. They enable engineers to actively shape and steer wavefronts by varying amplitude, phase, and polarization. They have very fine control over the behavior of electromagnetic waves. Metasurfaces enable flat, compact devices with performance comparable to, or sometimes better than, bulky traditional optics that require thick lenses, multilayers, or complex assemblies for diverse applications [1–6]. Through the appropriate design of the Dispersion, shape, and configuration of subwavelength meta-atoms, phase delay, amplitude change, and polarization conversion can be directly engineered on the metasurface itself. This multifunctional control has enabled the development of a metasurface technology that implements polarization converters and other novel optical devices [7–11]. Therefore, metasurfaces

will rapidly emerge as a platform for developing compact high-performance devices for next-generation applications such as integrated photonics, communications, imaging, and sensing [12–14]. With the increasing capabilities of metasurfaces, polarization control has become one of their most important functionalities. In particular, terahertz (THz) polarization converters have attracted considerable attention because they can provide compact control of electromagnetic polarization for imaging, spectroscopy, communications, and sensing applications. However, many conventional polarization converters rely on resonant metallic structures whose operating bandwidth, angular response, and fixed electromagnetic properties can limit their practical flexibility. The integration of actively tunable materials, particularly graphene, provides an additional degree of freedom, as its electrical conductivity can be adjusted via the chemical potential (Fermi level) without requiring physical modification of the metasurface geometry. Earlier studies have demonstrated graphene-assisted tunable polarization conversion and hybrid graphene–metal metasurfaces, establishing graphene as an effective material for dynamically controlling THz electromagnetic responses [15–18].

More recent approaches have investigated the coupling of polarization conversion with refractive-index sensing to detect analytes such as biomolecules or environmental pollutants, where small variations in the surrounding medium affect the metasurface's resonant frequency [19-23]. Terahertz sensing of multiple analytes, including cancer cells, malaria, antigens, and glucose, has been demonstrated using plasmonic, graphene-based, and refractive-index-sensitive biosensing devices [24–27]. Despite progress, it remains difficult to realize a single metasurface that achieves high polarization conversion efficiency, broadband operation, tunability, and sensing sensitivity. This encourages further work on design strategies to integrate these features into a single, coherent platform. More recently, the integration of polarization conversion with refractive-index sensing has received increasing attention. Several THz metasurface platforms have demonstrated the combined functionality of broadband polarization conversion and sensing, while graphene-assisted designs have further introduced electrical tunability. For example, a graphene-integrated reflective polarization converter reported in 2025 achieved a PCR above 90% over 10.408–21.524 THz and demonstrated a maximum refractive-index sensitivity of 3.40 THz/RIU [28]. Another graphene-integrated THz polarization converter reported broadband conversion over the range 9.461–15.707 THz, with a maximum sensitivity of 2.06 THz/RIU [29]. More recently, graphene-assisted reflective metasurfaces have been reported with operating ranges of 6.3–14.36 THz and 14.11–20.25 THz, combining broadband polarization conversion, Fermi-level tuning, and refractive-index sensing [30,31]. These studies demonstrate that combining polarization conversion, graphene tunability, and sensing is feasible; however, the reported structures differ substantially in their operating bands, geometric configurations, sensing schemes, angular responses, and conversion characteristics. Therefore, further investigation of compact reflective metasurfaces that simultaneously provide dual-band polarization conversion, graphene-enabled tunability, and refractive-index sensing remains relevant.

In this work, we propose and numerically investigate a compact graphene-integrated reflective metasurface for broadband THz polarization conversion and refractive-index sensing. The proposed structure consists of asymmetric aluminum resonators, a polyimide dielectric spacer, an aluminum ground plane, and a graphene layer that provides an additional electrical tuning mechanism. The proposed metasurface exhibits PCR values above 90% over two frequency bands, 6.108–10.773 THz and 11.648–14.051 THz, corresponding to a combined bandwidth of 7.068 THz. Within selected sub-bands, the PCR exceeds 96%, demonstrating strong cross-polarization conversion. The main contributions of this work are: (i) dual-band PCR above 90% over a total bandwidth of 7.068THz in a compact $13\times 13\times 3.7\mu m^3$. unit cell; (ii) graphene -based spectral tuning of the PCR cutoff frequencies; and (iii) refractive–index sensing by tracking the PCR cutoff frequencies, with a local maximum sensitivity of 3.5772THz/RIU and linear-fit sensitivities of 1.454 THz/RIU and 1.177THz/RIU. The response under oblique incidence is investigated from 0° to 45°; the spectral characteristics remain comparatively stable up to approximately 20°, whereas larger incidence angles produce noticeable resonance shifts and PCR degradation. Therefore, the angular analysis is used to characterize the practical angular response rather than to claim broadband angular robustness over the complete 45° range. The effect of graphene chemical potential is further investigated to establish the

electrical tunability of the proposed structure. Finally, the refractive-index sensing capability is evaluated over an RI range of 1.00–1.40 by monitoring the shifts in the lower and upper PCR cutoff frequencies. The resulting platform combines broadband polarization conversion, graphene-enabled spectral tunability, and refractive-index-based sensing within a compact reflective THz architecture.

## 2. Unit cell arrangement and its theory

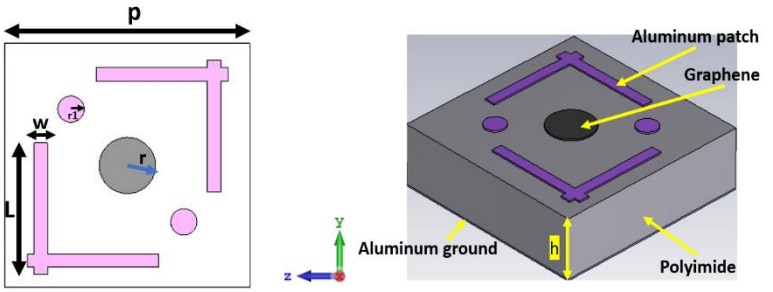


**(a)** **(b)**

**Fig. 1.** Unit cell: (a) Front view, (b) Perspective view

Fig. 1 demonstrates the design structure of the polarization rotator with both front view and 3-D representations of the basic unit cell. There are several layers that constitute the polarization converter, including an aluminum ground plane at the bottom, a polyimide dielectric in between, and graphene/aluminum radiators at the top. The multilayer structure is carefully selected to enhance interactions with incident electromagnetic waves and to achieve dynamic control of the response using tunable graphene. Table 1 describes and illustrates clearly the material and design requirements of the proposed structure. Aluminum was chosen for its high electrical conductivity ($3.56 \times 10^7$ S/m), which leads to high reflectivity and current efficiency. The polyimide spacer is used to provide the required stability and to reduce electromagnetic losses, with a loss tangent of 0.0027 and a relative permittivity of 3.5. These operating conditions — a graphene μ (C.P) of 0.1 eV, a $\sigma$ of 0.1 ps, and a temperature of 293 K — highlight the graphene layer's capability for active, external control of the metasurface response. An additional layer of the analyte can be incorporated into the metasurface to make the sensitive part work. This provides a good way to determine the refractive-index changes that cause changes in the spectral response

**Table 1**. Geometrical dimensions and material specifications of the proposed metasurface

| Geometrical Parameter | Symbol | Value(μm) | Material Parameter | Value(μm) |
|---|---|---|---|---|
| Unit cell Periodicity | p | 13 | Aluminum | 0.1 |
| Arm/Strip length | l | 7 | Polyimide | 3.7 |
| Arm/strip width | w | 0.7 | Graphene | 0.1 |
| Center circular radius | r | 1.5 | | |
| Circular radius | r1 | 0.3 | | |

The mechanism underlying polarization conversion in the proposed metasurface is illustrated in the functional diagram of Fig. 2. When an x-polarized incident wave interacts with the structure, it induces electric and magnetic field components within the aluminum strips, giving rise to surface currents on the resonator. This results in the conversion of polarization from one state to the other. This unbalanced arrangement of metal arms disrupts the structure's symmetry, thereby enhancing cross-polarization conversion. Moreover, the conductivity of the graphene layer is affected by external biases, thereby influencing the device's resonant condition. The performance of this design was simulated using CST Microwave Studio. Simulation results show that the presented device achieves high polarizer conversion performance and good sensitivity to RI changes. The proposed design is designed and simulated using Computer Simulation Technology (CST-2024), a finite element method-based software platform. The selected boundary conditions are open boundaries at Zmax and Zmin, and periodic boundaries along the unit-cell edges of the $x-$ and $y$ axes. The excitation of the designed structure has been done using the Floquet ports of the fundamental TE and TM modes.

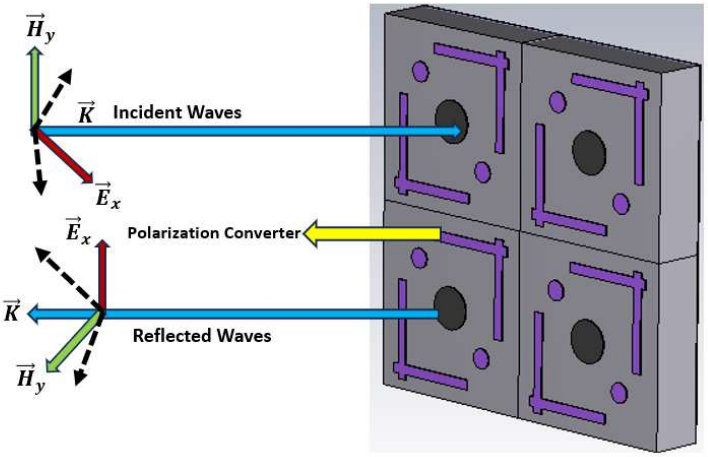


**Fig.2** Schematic illustration of the polarization-conversion mechanism

## 3. Numerical Results & Analysis

The reflection properties and PC effects of the design are depicted in Fig. 3. Fig. 3(a) shows the $R_{xx}$ and $R_{yx}$ cases, whereas Fig. 3(b) shows the PCR for the polarized input waves. For both horizontal and vertical plane EM waves, the reflection amplitude for x to x and x to y (co- and cross) is described as follows.

$$R_{yx} = \frac{|E_{ry}|}{|E_{ix}|} \quad (1)$$

$$R_{xy} = \frac{|E_{rx}|}{|E_{iy}|} \quad (2)$$

$$R_{xx} = \frac{|E_{rx}|}{|E_{ix}|} \quad (3)$$

$$R_{yy} = \frac{|E_{ry}|}{|E_{iy}|} \quad (4)$$

The PCR values can be obtained from the reflection coefficients by the formulae:

$$PCR_x = \frac{|R_{yx}|^2}{|R_{yx}|^2+|R_{xx}|^2} \quad (5)$$

$$PCR_y = \frac{|R_{xy}|^2}{|R_{xy}|^2+|R_{yy}|^2} \quad (6)$$

where Rxy or Ryx are the reflection coefficients of cross-polarized waves in the y and x polarizations, respectively. The simulation results show that the proposed metasurface structure operates efficiently over the frequency range 5-15 THz.

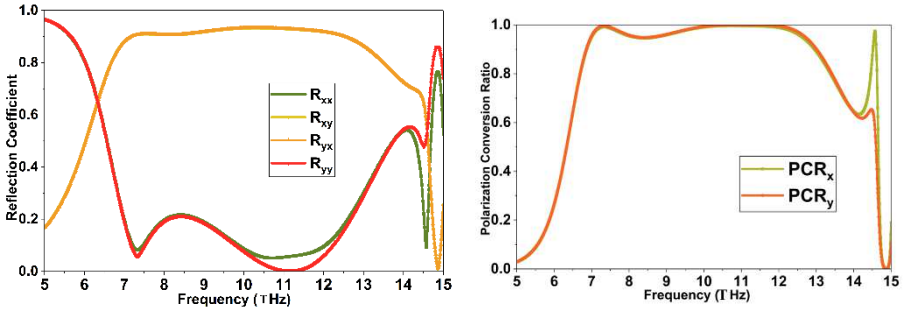


**(a)** **(b)**

**Fig.3** (a) Simulation Results of Co-and Cross-polarized, and (b) PCR

The suggested metasurface exhibits good broadband polarization-conversion characteristics, with a PCR exceeding 90% across two frequency bands: 6.108–10.773 THz and 11.648–14.051 THz. The combined bandwidth of these two operating bands comes to about 7.068 THz. The responses for $PCR_y$ and $PCR_x$ in the stated frequency intervals show good agreement, with the overall PCR value of 95.98%. Thus, the conversion efficiency of the proposed metasurface is successfully confirmed. Moreover, the PCR value exceeds 96% across three sub-bands: 6.236–6.920 THz, 8.069–9.860 THz, and 12.489–13.750 THz, yielding a total bandwidth of 3.736 THz. The overall PCR across these sub-bands is 98.31%, with a maximum of close to 99.95%. It can be concluded that the designed metasurface exhibits high PCE across a wide frequency range.

## 3.1 Oblique-Incidence Angular Stability

The polarization sensitivity of the proposed PC has been investigated to assess its effectiveness under oblique incidence. Fig. 4(b) shows a plot of PCR versus frequency at incidence angles ranging from 0° to 45 °. At $0^0$ incident angles, the proposed converter exhibits high PCR over a wide frequency band, with the main PCR properties occurring in the 8–13 THz range. At increasing incidence angles from $0^0$ to $20^0$, the spectral response is quite similar, but with some variations in PCR. Beyond $20^0$, greater angular dependence becomes evident, particularly within the resonant regions, where PCR demonstrates more pronounced reductions and wavelength shifts. The central high-conversion region, however, sustains a high PCR even at greater oblique angles, thereby implying a good degree of angular stability. At larger incidence angles of $30^0$, $40^0$, and $45^0$, more changes are evident, particularly at higher-frequency resonances, implying greater sensitivity of the polarization-conversion response to oblique illumination.

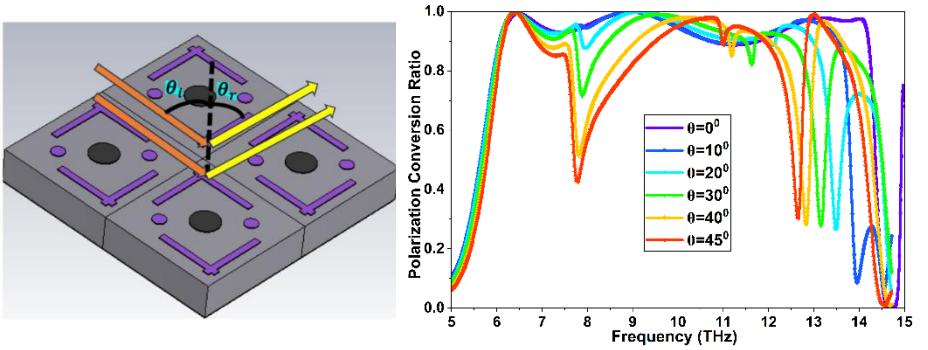


**Fig. 4**. (a) Schematic representation of the proposed metasurface under oblique incidence of an x-polarized wave. (b) Simulated PCR for incidence angles

This angle dependence arises from changes in the coupling process between the incoming electromagnetic wave and the asymmetric resonators as the angle of incidence increases. In other words, the amplitude-phase relationship of the orthogonal reflected waves varies with increasing angle of incidence, thereby making the efficiency of the proposed metasurface angle-dependent.

## 3.2 Parametric analysis

To improve the efficiency of polarization conversion in the proposed metasurface, a comprehensive parametric study is conducted by varying the arm length l, arm width w, periodicity p, and substrate thickness h, as shown in Fig. 5(a–d). Firstly, the effect of the arm length l is studied for (l=6, 6.5, 7, and 8 µm. Changes in the arm length, l, led to notable differences in resonant frequencies and in the PCR graph. Among the values investigated, l=7 µm yields optimal broadband performance of the polarizer. The dependence on the arm width is also considered, with values of w = 0.5, 0.7, 0.9, and 1 µm. Changes in width influence resonant performance, particularly in the high-frequency range, with w = 0.7 µm exhibiting broad, smooth high-PCR. Next, the periodicity of the unit cell is modified from p=13 to 16 µm. PCR at p=13 µm exhibits a broad, smooth high-PCR region, while

high values show pronounced fluctuations in the high-frequency range.

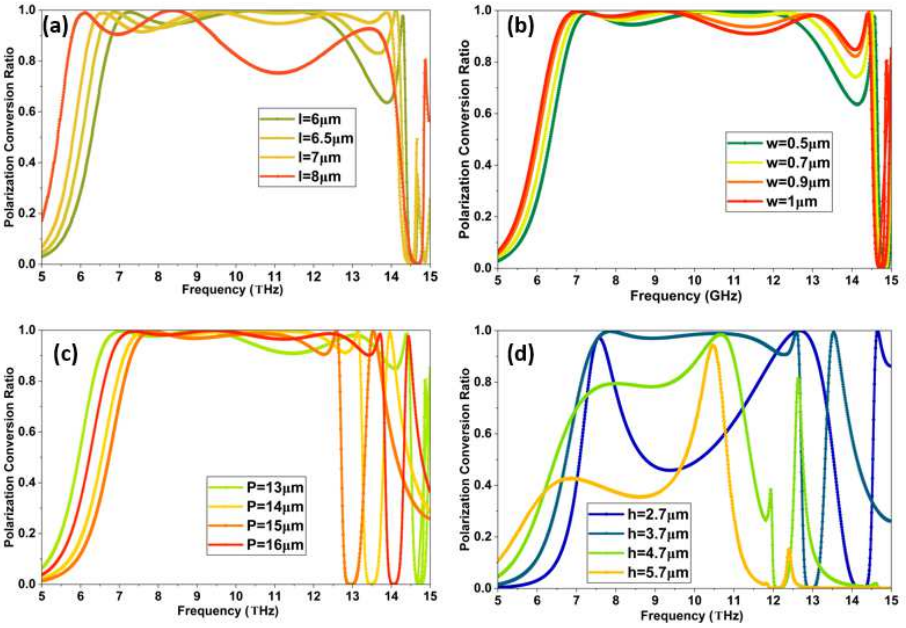


**Fig.5** Parametric analysis (a) Arm length l, (b) Arm width w, (c) Periodicity P, and (d) Substrate thickness

Finally, the substrate thicknesses are set to h = 2.7, 3.7, 4.7, and 5.7 μm. The change in substrate thickness significantly affects the resonance distribution and properties of PCR, with h = 3.7μm exhibiting a relatively large and stable range of high-conversion response. As a result of the parametric analysis, the optimal geometric parameters for PCR are determined to be L = 7 μm, w = 0.7 μm, p = 13μm, and h = 3.7 μm.

# 4. Graphene-Enhanced Polarization Conversion Performance

## 4.1 Graphene-Enabled Electrical Tunability

The advantage of using graphene to construct the polarization converter is that the device's electromagnetic behavior can be dynamically controlled. Unlike traditional metallic elements, whose properties do not change and remain in their resonant states, graphene's properties can be tuned to change its electromagnetic behavior. The reason is the ability to control the surface conductivity, which can be varied via chemical potential. Thus, the interaction between the terahertz wave and the metasurface can be changed. The frequency-dependent surface conductivity of graphene is calculated using the Kubo formalism, which accounts for both intraband and interband contributions. In the considered terahertz frequency range, the intraband contribution is dominant under the selected chemical-potential conditions. The graphene conductivity is controlled through the chemical potential $E_F$, while the relaxation time and temperature are fixed at $\tau = 0.1$ps and $T = 293$K, respectively. The total conductivity of graphene can be defined as follows [32, 33]:

$$\sigma(\omega) = \sigma_{inter}(\omega) + \sigma_{intra}(\omega) \tag{7}$$

At lower frequencies, the intraband contribution dominates the terahertz frequency range, where $h\omega << E_f$. This coefficient depends mostly on the $\mu$ and the σ, can therefore be described with the help of a Drude form:

$$\sigma_{intra}(\omega) = \frac{ie^2 E_f}{\pi h^2(\omega + i\tau^{-1})} \quad (8)$$

where $E_f$, ω, τ, e, and h represent the Fermi level ($\mu$), angular frequency, relaxation time, electron charge, and reduced Planck's constant, respectively. As $E_f$ increases, the intraband (Drude) conductivity increases and interband transitions are suppressed by Pauli blocking for $h\omega < 2E_f$ leading to changes in graphene's electrical conductivity. As a result, the surface impedance and the resonance condition of the metamaterial structure are affected.

The relative contributions of these terms are tunable by the chemical potential, thereby enabling tunable metasurface resonances. Fig. 6(a) presents the variation in polarization conversion ratio corresponding to two graphene Fermi-level values, 0.1 eV and 1.0 eV. The simulation results show that the designed PC retains a high PCR within the two operating bands for both Fermi-level values. Figs. 6(b) and (c) show magnified insets of the lower- and higher-frequency regions, respectively, to demonstrate the small shifts induced by the chemical potential adjustment, which do not significantly affect the polarization conversion ratio. To quantitatively assess the spectral tunability induced by graphene, the frequency shifts at a PCR level of 0.80 were extracted from the magnified responses shown in Fig. 6(b) and (c). In the lower-frequency region, increasing the graphene Fermi level from $E_F = 0.1$to 1.0eV shifts the 0.80-PCR cutoff frequency from approximately 5.79 THz to 6.25 THz, corresponding to a frequency shift of about 0.46 THz (≈7.9%). In the higher-frequency region, the corresponding cutoff shifts from approximately 14.36 THz to 14.75 THz, giving a frequency shift of about 0.39 THz (≈2.7%). These results demonstrate that the chemical potential of graphene provides measurable spectral tuning while maintaining a high polarization-conversion response.

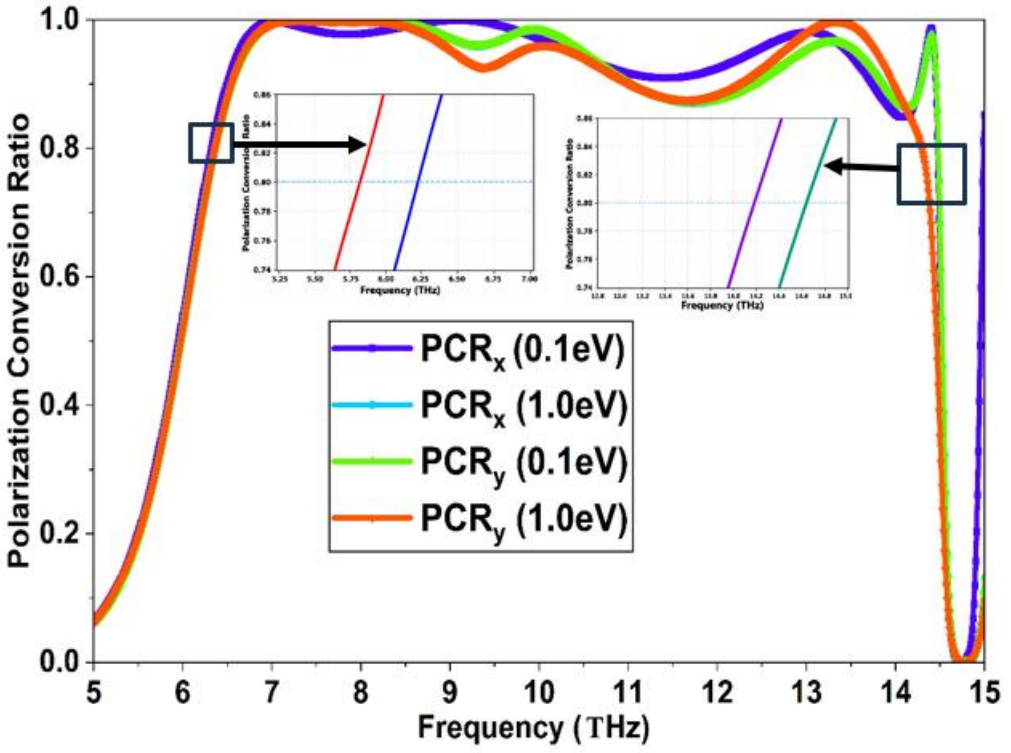


**Fig. 6.** (a) Effect of graphene Fermi-level variation from 0.1 to 1.0 eV on the polarization conversion ratio. (b and c) Magnified view of the low and high-frequency regions,

Results from this simulation confirm graphene's effectiveness in enabling tunable devices. The ability to adjust the device is very important for many terahertz applications, as it enables changing the operating frequency in response to factors such as fabrication tolerances and environmental conditions.

## 4.2 Robustness of Polarization Conversion Against Graphene Relaxation Time and Temperature Fluctuations

To test the effectiveness and stability of the suggested polarization conversion method, the effects of graphene relaxation time τ and operating temperature T on the PCR were investigated; the results are presented in Fig. 7

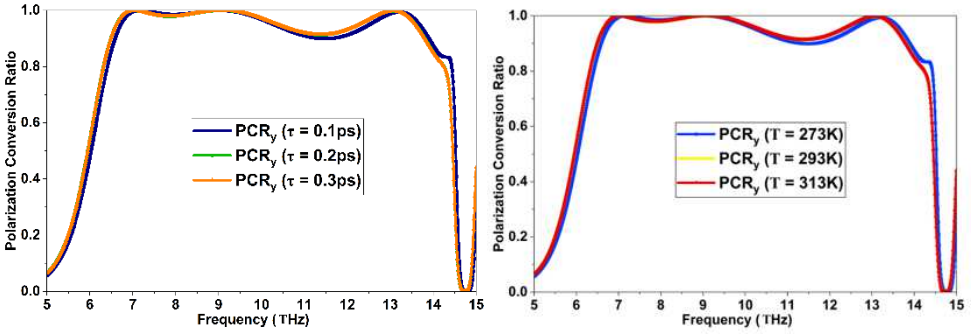


**(a)** **(b)**

**Fig.7 PCR** of (a) relaxation time and (b) Temperature

It can be seen from Fig. 7(a) that the PCR is almost insensitive to variations in relaxation time in the range of 0.1 ps to 0.3 ps, indicating that the converter's performance is only weakly dependent on this parameter. Likewise, Fig. 7(b) shows that the polarization conversion performance is almost unchanged with temperature over the range 273 K to 313 K. Within the operating bands, the PCR remains high (above 90%) for all the considered relaxation times and temperatures

## 5. Reflection- and Phase-Difference-Based Analysis of the Polarization-Conversion Mechanism

To evaluate the performance of the proposed polarization converter, the unit cell's reflection coefficients and phase-difference characteristics were examined. As depicted in Fig. 8(a), a coordinate transformation defines u and v as the new polarization axes relative to the original x- and y-axes. When the incident electric field Ei interacts with the metasurface, its components are reflected along the u- and v-directions.

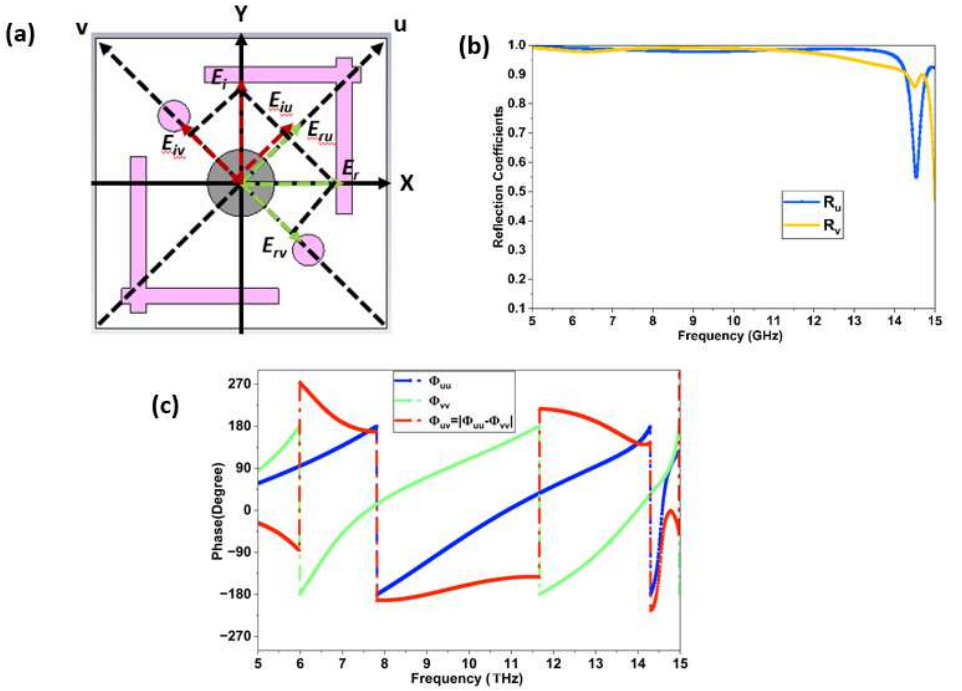


**Fig. 8.** (a) decomposition of the wave into components along the u- and v-axes, (b) Reflectivity, and(c) Reflectivity phase

Reflected-field components are important parameters for analyzing the efficiency of the cross-polarization technique shown in Fig. 8(b). The co-polarized reflection components are strongly suppressed, whereas the cross-polarized reflection components remain high over the polarization-conversion bands. This confirms that the metasurface can govern the polarization state of the reflected wave through its inherent structural properties. Efficient polarization conversion requires comparable amplitudes of the two orthogonal reflected field components together with an approximately 180° phase difference. Under this condition, the co-polarized components undergo destructive interference, whereas the cross-polarized components interfere constructively, resulting in a high PCR. Furthermore, phase behavior plays an important role in the polarization-conversion process. It should be emphasized that the phase results depicted in Fig. 8(c) are provided only to elucidate the fundamental conversion mechanism and do not imply a standalone phase-modulation function. From Fig. 8(c), we can see that the phase difference $\Delta\varphi$ is always close to 180° in the whole band. This is an important factor in generating the polarization rotation process. With the nearly 180° phase difference, constructive interference occurs for the cross-polarized wave while the co-polarized wave experiences destructive interference.

## 6. Surface Current Distribution

Surface current distributions for the patterned aluminum resonator are shown in Fig. 9 at three frequencies: 6.5 THz, 9 THz, and 12.5 THz, each corresponding to a specific point in the broadband cross-polarization band. This structure consists of two L-shaped metallic arms placed diagonally in the top-right and bottom-left quarters of the unit cell, and two large circular structures with two smaller circles within the opposing quarters. The color coding indicates the magnitude of the currents, with darker colors indicating strong field confinement, while black arrows denote the direction of the

instantaneous current distribution within the arms.

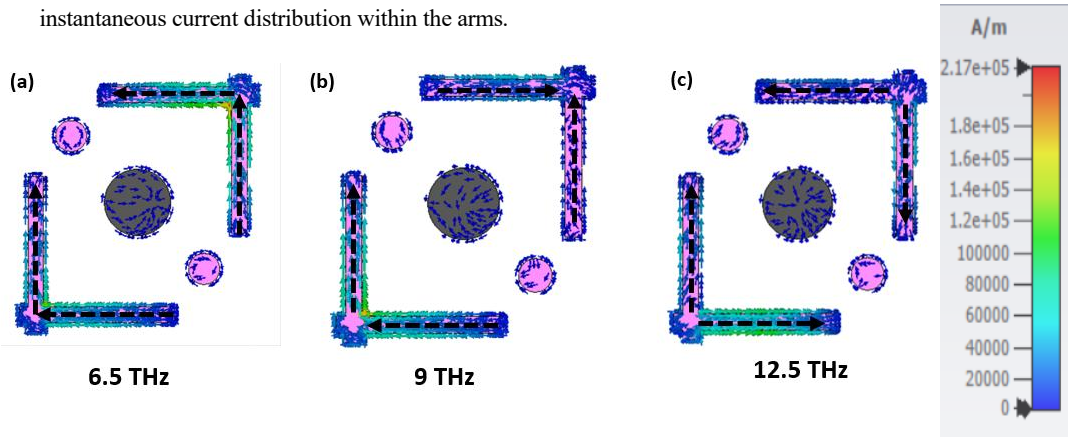


**Fig. 9** Surface current distribution: (a) 6.5 THz, (b) 9 THz, and (c) 12.5 THz

In the case of 6.5 THz [Fig. 9(a)], it can be observed that the electric current moving in the upper and right parts converges in the direction of the top-right junction point, while the electric current moving in the lower and left parts is directed to the bottom-left junction point, thus forming an antisymmetric current flow between the two L-shaped structural parts. The asymmetry in the current flow produces a net circulating current, resulting in magnetic dipole resonance phenomena, which are the main reason for the successful conversion of the polarization state to the orthogonal one. In the case of 9 THz Fig. 9(b), the current distribution pattern is quite similar; however, the electric current density is noticeably higher at the bottom-left junction point. With increasing frequency up to 12.5 THz (Fig. 9(c)), the current orientation changes in the right and bottom arms, whereas the top and left arms retain their original orientation, in contrast to the situation at lower frequencies. Such a change indicates that a higher-order current loop has been established, with the loop oriented antiparallel, which is necessary for magnetic resonance. In all three frequency ranges studied, the current exhibits a consistent vortex orientation within the central circular loop, indicating that the loop serves as a frequency-independent stabilizer. The smaller circular regions, on the other hand, indicate reduced circulating currents, resulting from near-field coupling between the two L-shaped arms and contributing minimally to the overall resonance strength. Collectively, the currents illustrate that the L-shaped arms are the primary sources of resonances and polarization transformations, while the frequency variation along their paths is responsible for the device's operation.

To further investigate the polarization-conversion mechanism, the electric-field distributions of the proposed metasurface are examined at 6.5, 9, and 12.5 THz for phase angles of 0°, 90°, 180°, and 270°, as presented in Table 2. At 6.5 THz, the electric field is mainly concentrated around the metallic arms and resonant regions of the asymmetric structure. As the phase angle varies, the field distribution changes progressively, indicating a phase-dependent electromagnetic response. At 9 THz, stronger field localization is observed around different portions of the resonator, demonstrating the contribution of the resonant elements to the polarization-conversion response. At 12.5 THz, the electric field is redistributed around the resonator arms and central region, indicating the contribution of the higher-frequency resonance. The approximately opposite-field states observed at 0 to the ring operator and 180 to the ring operator, together with the corresponding quadrature states at 90 to the ring operator and 270 to the ring operator, demonstrate the phase evolution of the induced electric response. Such phase-dependent redistribution of the electric field contributes to the generation of the orthogonal field component and hence supports the polarization-conversion behavior of the proposed metasurface.

**Table2.** Electric-field cross-polarized rotation behavior. at 6.5, 9, and 12.5 THz.

| Frequency | Phase Angle | | | |
|---|---|---|---|---|
| | 0º | 90º | 180º | 270º |
| 6.5THz | 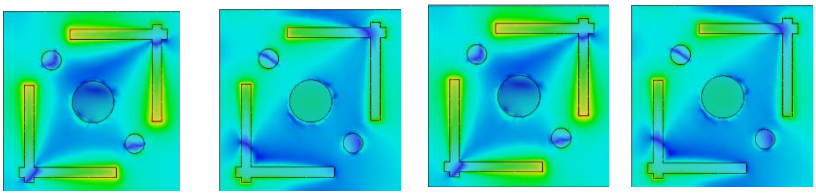 | | | |
| 9 THz | 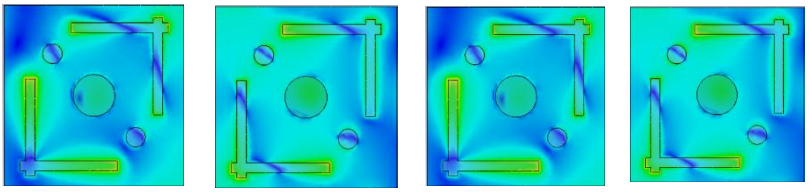 | | | |
| 12.5 THz | 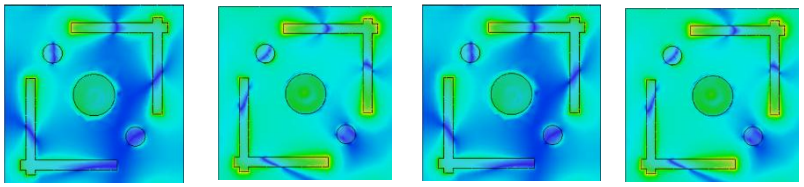 | | | |

## 7. Comparative Analysis with Previously Reported Designs

Table 3 compares the proposed polarization converter with previously reported polarization converters. From the results obtained, it is evident that most existing designs have a relatively narrow operational bandwidth and limited configurability, with polarization conversion capability tailored to specific frequency ranges. However, the designed graphene-based metasurface exhibits a broader operating band in the terahertz regime and an excellent polarization conversion ratio. As shown in Fig. 3(b) , the behavior of both $PCR_X$ and $PCR_y$ is quite consistent in the main conversion region, indicating that the PCR of the proposed design is relatively independent of polarization in both orthogonal directions. The suggested structure has a PCR greater than 90% over 6.108-10.773 THz and 11.648-14.051 THz, with a total absolute bandwidth of 7.068 THz. Moreover, the graph shows that the value of PCR remains close to unity over a considerable portion of this frequency range. In the suggested design, a small unit cell with 13 μm × 13 μm dimensions and a 3.7 μm-thick substrate forms a subwavelength structure for terahertz polarization manipulation. The unit-cell dimensions in Table 3 are normalized to the free-space wavelength $\lambda_o$ at the lowest operating frequency (6.108 THz). Using graphene introduces an additional variable into the system, enabling electrical control of the electromagnetic response without altering the broadband polarization-conversion principle. This way, the presented metasurface offers a broad operating bandwidth, high polarization conversion efficiency,

compact size, and electrical tunability, thereby overcoming some of the limitations of conventional polarization converters.

**Table 3.** Comparative analysis of the proposed design with previously reported designs

| Ref | Size of Unit Cell ($\lambda_o$) | Operating Frequency (THz) | Operating Bandwidth | PCR | Tunable |
|---|---|---|---|---|---|
| **[23]** | 0.19 × 0.19 × 0.07 | 2.12–5.16 | 3.04 THz | < 90% | No |
| **[36]** | 0.23 × 0.23 × 0.06 | 0.65–1.45 | 0.80 THz | < 80% | No |
| **[37]** | 0.10 × 0.10 × 0.10 | 0.20–1.00 | 0.80 THz | < 80% | No |
| **[38]** | 0.15 × 0.15 × 0.10 | 0.38–1.07 | 0.69 THz | < 80% | No |
| **[39]** | 0.24 × 0.24 × 0.08 | 3.80–8.25 | 4.45 THz | <90% | No |
| **[40]** | 0.12 × 0.12 × 0.06 | 3.12–9.60 | 6.48 THz | < 80% | No |
| **[41]** | 0.27× 0.27× 0.12 | 8.119–17.826 | 9.707 THz, 8.199 THz | <90% <96% | Yes |
| **Proposed Design** | 0.265× 0.265× 0.075 | **6.108-10.773, 11.648-14.051** | **7.068** | **> 90%** | **Yes** |

Most reported graphene-based biosensors operating in the terahertz regime follow the architecture of either absorptive or resonant sensors, whose outputs are primarily shifts in resonance peaks due to refractive-index variation [34, 35]. In this study, sensing via the refractive index is pursued, but implemented here by tracking the PCR cutoff frequencies of PC metasurface. In this system, sensing can be accomplished by monitoring changes in the resonant cut-off frequency, while simultaneously enabling broadband polarization conversion via reflection in the terahertz range. The aluminum layer provides broadband polarization conversion via magnetic resonance, while the graphene layer enables electrical tuning without degrading polarization-conversion performance.

## 8. Biosensing Mechanism Based on Refractive-Index Variation

The designed polarization-conversion metasurface can also serve as an efficient biosensor, owing to the strong interaction between analyte molecules and the concentrated electromagnetic field generated by the resonators. When an analyte with a different refractive index comes into contact with the surface, it modifies the effective dielectric environment of the graphene-loaded structure. This leads to changes in the biosensor's resonance properties, causing variations in its optical response.

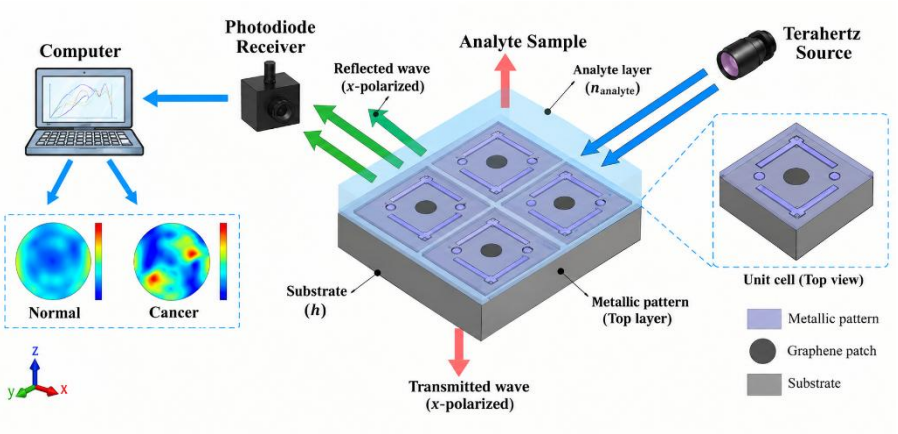


**Fig.10 Schematic of the proposed biosensing mechanism**

Fig. 10 shows the working principle of the proposed sensing technique. The x-polarized terahertz wave produced by the source falls onto the metasurface, and the addition of the sample causes the reflection to change. This changed reflection signal is detected by the photodiode and fed into the computer. As a result, the observable changes in the signal enable differentiation between healthy and pathological biological samples, such as healthy versus cancerous tissue

## 8.1 Refractive-Index-Dependent Sensing Response

The sensing performance of the proposed metasurface is evaluated for refractive-index sensing by examining the behavior of the polarization conversion ratio (PCR) across different refractive indices of the surrounding analyte medium. The PCR spectra show a progressive shift with increasing refractive index, as shown in Fig. 11, indicating a strong sensitivity of the polarization-conversion response to the dielectric properties of the surrounding medium. The lower and upper cutoff frequencies, $F_L$ and $F_H$ are observed at the 80% PCR threshold, as shown in the enlarged views in Fig. 11(b) and (c), respectively. An 80% PCR threshold is selected to define the sensing bandwidth boundaries because it provides a consistent spectral criterion within the high-conversion region while avoiding ambiguity associated with the rapid spectral transitions near the band edges. The same threshold is applied to all refractive-index conditions to ensure consistent extraction of the lower and upper cutoff frequencies. The lower cut-off frequency $F_L$ decreases from 5.9727 THz for n=1.00 to 5.3458 THz for n=1.40, and the upper cut-off frequency $F_H$ changes from 14.1739 THz to 13.6765 THz within the same refractive-index range, as shown in Table 4. Consequently, there is a uniform shift of both cutoff frequencies toward lower frequencies as the refractive index increases.

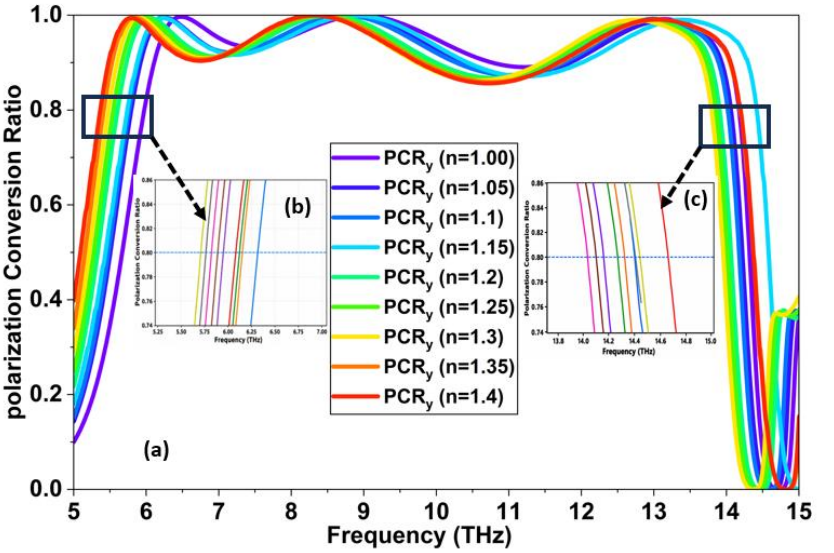


**Fig. 11.** (a) PCR response for varying refractive-index values; (b) and (c) show zoomed-in views of the lower- and higher-frequency cutoffs, respectively, corresponding to the 80% PCR level.

The sensitivity was first evaluated locally between consecutive refractive-index values using $S = |\Delta f/\Delta n|$. The maximum local sensitivity was obtained as 3.5772 THz/RIU for the lower cutoff frequency $F_L$and 2.2234 THz/RIU for the upper cutoff frequency $F_H$Both occur over the first refractive-index interval from 1.00 to 1.05. The local sensitivity varies noticeably between consecutive intervals: 0.6012 THz/RIU for n=1.05-1.10, which is attributed to the finite frequency resolution of the cutoff extraction at the 80% PCR level; the fitted values are therefore more representative of the overall sensing performance. To further evaluate the overall linearity of the sensing response, linear regression was performed using all nine refractive-index points from 1.00 to 1.40, as shown in Fig. 12(a) and (b). The lower cutoff frequency follows $F_L = -1.4538n + 7.3677$with $R^2 = 0.9803$, corresponding to an overall fitted sensitivity of 1.454 THz/RIU. Similarly, the upper cutoff frequency follows $F_H = -1.1773n + 15.3228$with $R^2 = 0.9928$, giving an overall fitted sensitivity of 1.177 THz/RIU. The negative slopes indicate a redshift of both cutoff frequencies as the refractive index increases. The high $R^2$values indicate a strong linear correlation over the investigated range of refractive index.

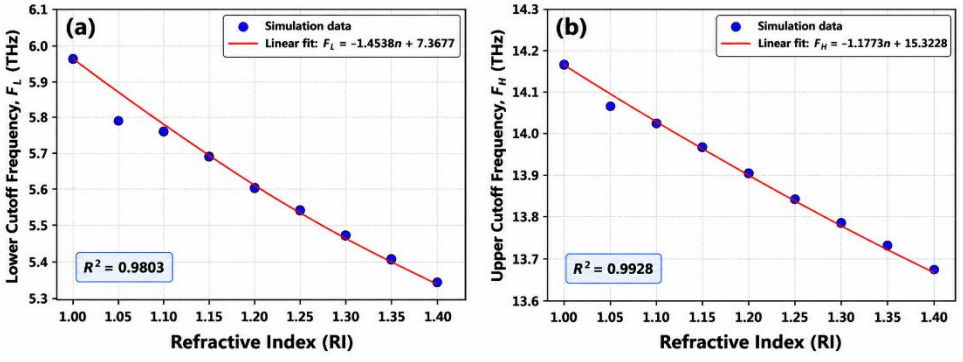


**Fig. 12**. Linear fitting of the PCR cutoff frequencies as a function of refractive index: (a) lower cutoff frequency $F_L$, and (b) upper cutoff frequency $F_H$.

**Table 4.** Variation of resonance frequencies and sensitivity with refractive index.

| *Refractive Index* | *Lower Frequency* | *Sensitivity (THz/RIU)* | *Higher Frequency* | *Sensitivity (THz/RIU)* |
|---|---|---|---|---|
| 1.00 | 5.9727 | ------- | 14.1739 | ------ |
| 1.05 | 5.7938 | 3.5772 | 14.0627 | 2.2234 |
| 1.10 | 5.7638 | 0.6012 | 14.0186 | 0.8829 |
| 1.15 | 5.6893 | 1.4893 | 13.9682 | 1.0080 |
| 1.20 | 5.6053 | 1.6796 | 13.9057 | 1.2500 |
| 1.25 | 5.5456 | 1.1954 | 13.8546 | 1.0220 |
| 1.30 | 5.4788 | 1.3345 | 13.7937 | 1.2175 |
| 1.35 | 5.4138 | 1.3005 | 13.7364 | 1.1474 |
| 1.40 | 5.3458 | 1.3607 | 13.6765 | 1.1963 |

Refractive index-dependent frequency shifts create a detectable spectral feature enabling the identification of changes in the dielectric environment surrounding the metasurface. The systematic shift of the PCR cut-off frequencies demonstrates the ability of the proposed configuration for terahertz refractive-index sensing and biosensing applications, in which changes in an analyte's dielectric properties can be detected via the corresponding frequency shift.

## 8.2 Detection of Multiple Analytes Using the Proposed Biosensor

The proposed biosensor's detection capability relies upon the distinctions in dielectric characteristics between reference and test specimens. Alterations in cell density, moisture content, solute concentration, and chemical composition cause variations in the refractive index of the medium, resulting in shifts in the polarization resonance frequencies $F_L$ and $F_H$.

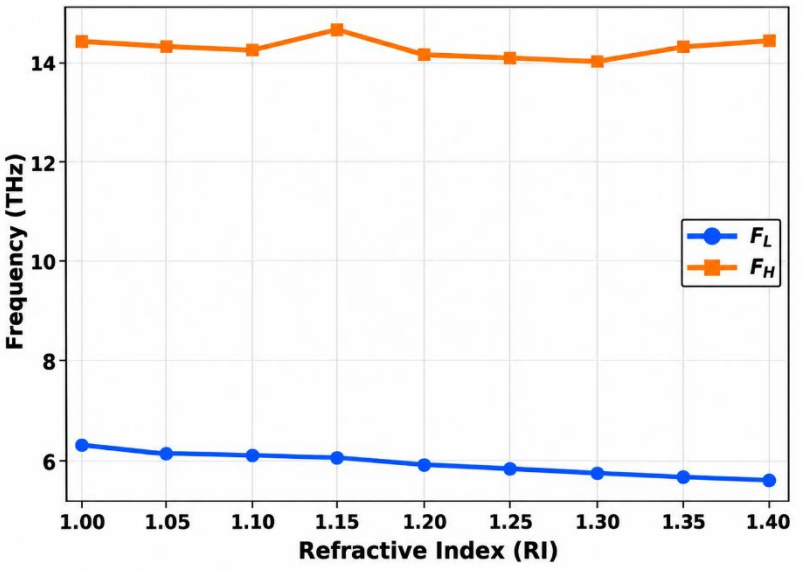


**Fig. 13.** Refractive-index-dependent shifts in $F_L$ and $F_H$.

To investigate this phenomenon, the refractive indices of several representative biological materials have been collected from various sources and incorporated into the simulation procedure [42–48]. It

should be noted that most of the literature values [42-48] were measured at optical wavelengths, whereas biological samples generally exhibit a higher refractive index and strong absorption in the THz range; these values are therefore used only as representative inputs, and the absolute frequency shifts at THz frequencies must be confirmed with measured THz complex permittivity. The hemoglobin concentration of 40g/L (n=1.430) lies outside the simulated range of n =1.00-1.40 and is therefore not evaluated. Given that the refractive index of biological tissues may depend on several parameters, including moisture level, temperature, measurement wavelength, and sample preparation, the presented values represent only input data for the numerical investigation. Notable variations in both FL and FH were recorded across several biological conditions, including healthy versus malaria-infected blood, pure water versus a 25% glucose solution, healthy versus cancerous breast tissue, and hemoglobin concentrations ranging from 10 to 40 g/L. Therefore, the results reported in Table 4 should be interpreted as a simulation-based comparative analysis rather than an actual diagnostic outcome. The results demonstrate that the proposed metasurface can distinguish different refractive-index conditions associated with representative biological samples in numerical simulations.

**Table 5**. Comparison of refractive index, resonance frequency, and sensitivity values for the selected biological samples.

| **Sample** | **State** | **RI** | $F_L$ | **Sensitivity $F_L$(THz/RIU)** | **$F_H$** | **Sensitivity $F_H$(THz/RIU)** |
|---|---|---|---|---|---|---|
| **Blood** | Healthy | 1.399 | 5.3472 | 1.1980 | 13.6777 | 1.1980 |
| | Malaria | 1.373 | 5.3825 | | 13.7088 | |
| **Water** | Normal | 1.3198 | 5.4531 | 1.3142 | 13.7710 | 1.1583 |
| | 25% Glucose | 1.3594 | 5.4010 | | 13.7251 | |
| **Breast** | Healthy | 1.385 | 5.3662 | 1.3600 | 13.6945 | 1.1980 |
| | Cancerous | 1.399 | 5.3472 | | 13.6777 | |
| **Hemoglobin** | 10 g/L | 1.340 | 5.4268 | — | 13.7479 | — |
| | 20 g/L | 1.360 | 5.4002 | 1.3300 | 13.7244 | 1.1720 |
| | 30 g/L | 1.390 | 5.3594 | 1.3600 | 13.6885 | 1.1980 |
| | 40 g/L | 1.430 | — | — | — | — |

This finding is further reinforced by the sensitivity values reported in Table 5, which show that both $F_L$ and $F_H$ respond strongly and nearly linearly to refractive-index variations, with $F_L$ exhibiting greater sensitivity than $F_H$.

## 9. Fabrication process and geometrical precision

The proposed polarization converter is readily integrable into common microfabrication processes used to fabricate terahertz devices [49, 50]. The fabrication process starts with metal film deposition on the substrate, forming a metallic ground plane that acts as a mirror, preventing wave transmission. A polyimide insulating layer is applied by spin coating and then annealed in a thermally controlled atmosphere. After that, the second aluminum layer is deposited on top of the polyimide and patterned into the required resonator shape using high-resolution lithography (electron-beam or deep-UV lithography, since the smallest features w = 0.7 μm and r1= 0.3 μm are below the resolution of conventional photolithography; the non-patterned areas are etched [51-53]. After obtaining the resonator pattern, a graphene monolayer is transferred onto its surface, enabling frequency tuning via voltage-dependent changes in graphene conductivity [54–57]. It should be noted that reaching $E_f$ = 1eV by electrostatic gating through a 3.7$\mu m$ A polyimide layer would require a bias of the order of 10 kV, which is not practical; ionic-liquid/ionic-gel gating or a thin, separate gate dielectric is more suitable, and the $E_f$ range in Section 4.1 should be regarded as a numerical study of the achievable tuning. In practical implementation, the graphene layer is transferred through an aqueous polymer-assisted technique, followed by removal of the residual polymer support and subsequent drying of the graphene film to prevent wrinkling and surface contamination. The electrical tuning is achieved by connecting the graphene layer to biasing electrodes near the active part of the metamaterial, with the ground plane, made of aluminum, serving as the counter electrode. The analyte thickness is controlled using a spacer-based microfluidic sensing channel with a height of 1 μm.

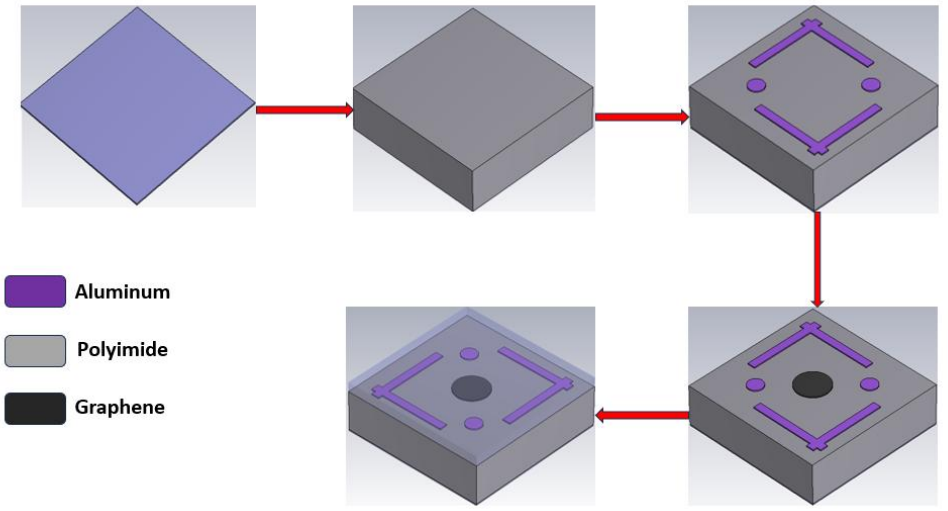


**Fig. 14.**. Schematic fabrication flow: aluminum ground plane to graphene-integrated sensing structure.

The approach helps ensure that a consistently maintained analyte layer remains on the sensor surface during the sensing process. The deposition of the analyte layer onto the graphene-modified sensor yields a fully functional sensor that detects changes in the index of refraction. As such, the next step in the process would be to move from the basic design to a fully functional graphene-modified sensing system. According to the computer simulation results, the design can sustain the broadband polarizer properties and ensure functional sensing even in the presence of small manufacturing errors.

## 10. Comparative analysis of the proposed terahertz biosensing platform with existing approaches

To assess the efficiency and applicability of the biosensor, a comparative study was conducted with several existing terahertz biosensors. The results of this study are presented in Table 5, with particular attention to sensitivity characteristics and multi-disease detection capability. Previous research focused mainly on the design of a biosensor for determining the refractive index using metal (gold, copper) transmitters, reflectors, and absorbers. Even though all those configurations were highly useful, their sensitivity was always less than 1 THz/RIU. However, despite recent sensors exhibiting considerable sensitivity (up to 1.53 THz/RIU for some aluminum-polyimide structures), they are designed solely for biosensing. The maximum local sensitivity of the proposed design (3.577 THz/RIU, obtained between n=1.00 and 1.05) is comparable to that of the best graphene -integrated PCR-based sensors reported recently (3.40THz/RIU [28]), wherease over the whole range n=1.00-1.40 the linear-fit sensitivities are 1.454THz/RIU ($F_L$) and 1.177 THz/RIU ($F_H$), which is comparable to those of the other aluminimum-polyimide sensors (1.53THz/RIU [63] and 1.67THz/RIU [41]). The advantage of the proposed design therefore lies in combining a compact init cell ($13\times 13 \times 3.7\mu m^3$), dual-band broadband polarization conversion and graphene tunability in a single structure, rather than in a record sensitivity. Moreover, in numerical simulations, the device can distinguish the refractive-index changes associated with several representative biological samples; clinical diagnostic capability would require experimental validation using terahertz spectroscopy. This means the proposed device is relatively sensitive compared with existing devices and can diagnose a wider range of diseases.

**Table 5.** Comparative analysis of the proposed terahertz biosensor and previously reported sensing platforms.

| Ref | Device Function | Unit Cell Size (μm³) | Materials System | Sensitivity (THz/RIU) | Year |
|---|---|---|---|---|---|
| [58] | Refractive-Index sensor | 94 × 94 × 65 | Gold-Silicon | 0.28 | 2020 |
| [59] | Terahertz Transmitter | 90 × 90 × 16 | Gold-Quartz | 0.28 | 2021 |
| [60] | Reflector element | 300 × 300 × 350 | Copper-Quartz | 0.05 | 2022 |
| [61] | Absorber | 100 × 100 × 8.6 | Gold-GaAs | 0.08 | 2023 |
| [62] | Biosensor | 20 × 20 × 4.2 | Gold-Polyimide | 0.68 | 2024 |
| [36] | Biosensor | 12 × 12 × 6.36 | Gold-Polyimide | 0.95 | 2025 |
| [63] | Biosensor | 18 × 18 × 6.2 | Aluminum-Polyimide | 1.53 | 2025 |
| [41] | PCR-based Biosensor | 10 × 10 × 4.6 | Aluminum-Polyimide-Graphene | 1.67 | 2026 |
| **This Work** | **PCR Biosensor** | **13 × 13 × 3.7** | **Aluminum-Polyimide-Graphene** | **3.577** | **2026** |

### Conflict of Interest

The authors declare no known conflicts of interest that could influence the work described in this study.

**Statement of Funding**

No specific grant from a public, private, or nonprofit funding organization was obtained for this study.

**Statement of Data Availability**

Upon reasonable request, the corresponding author will provide the data that support the study's conclusions.

**Statement of Ethics**

Since there are no human subjects, human data, or human participants in this study, ethical approval was not needed.

## 11. Conclusion

In this work, we demonstrate a small graphene-integrated reflective metasurface for refractive-index sensing and dual-band broadband terahertz polarization conversion. The proposed structure with an average PCR of 95.98% achieves PCR>90% over 6.108–10.773 THz and 11.648–14.051 THz with a total bandwidth of 7.068 THz. Moreover, a PCR above 96% is obtained across three sub-bands, with a total bandwidth of 3.736 THz, an average PCR of 98.31%, and a maximum of nearly 99.95%. The polarization-conversion response remains relatively stable for incidence angles up to approximately 20°, while noticeable spectral shifts and PCR degradation occur at larger incidence angles. The presence of graphene introduces electromagnetic tunability while preserving effective polarization conversion through chemical-potential tuning. For analyte indices from 1.00 to 1.40, consistent redshifts of the lower and upper PCR cutoff frequencies are observed in refractive-index sensing, yielding maximum local sensitivities of 3.5772 THz/RIU and 2.2234 THz/RIU, respectively (linear-fit sensitivities: 1.454THz/RIU and 1.177 THz/RIU). The distinct spectral responses of the relevant biological and aqueous materials further illustrate the proposed platform's potential for THz refractive-index sensing and multifunctional biosensing.

## Reference

1. S.B. Glybovski et al., Metasurfaces: from microwaves to visible. Phys. Rep. 634, 1–72 (2016)
2. S. Zahra et al., Electromagnetic metasurfaces and reconfigurable metasurfaces: a review. Front. Phys. 8, 593411 (2021)
3. H.-T. Chen, A.J. Taylor, N. Yu, A review of metasurfaces: physics and applications. Rep. Prog. Phys. 79(7), 076401 (2016)
4. Q. Wei et al., Optical wavefront shaping based on functional metasurfaces. Nanophotonics. 9(5), 987–1002 (2020)
5. L. Xiong, M. Xiaoliang, L. Xiangang, Principles and applications of metasurfaces with phase modulation. Opto-Electronic Eng. 44(3), 255–275 (2017)
6. M. Beruete, I. Jáuregui-López, Terahertz sensing based on meta-surfaces. Adv. Opt. Mater. 8(3), 1900721 (2020)

7. T. Cai et al., High-efficiency and full-space manipulation of electromagnetic wave fronts with metasurfaces. Phys. Rev. Appl. 8(3), 034033 (2017)

8. Q. Wang et al., Metasurface-assisted terahertz sensing. Sensors 23, 5902 (2023). https:/ /doi.or g/10.33 90/s2 3135902

9. Z. Shen, D. Huang, A review on metasurface beam splitters. Nanomanufacturing. 2(4), 194–228 (2022)

10. Q. He, S. Sun, L. Zhou, Tunable/reconfigurable metasurfaces: physics and applications. Research. 2019, 1–16 (2019). https://doi.org/10.34133/2019/1849272 11.

11. L. Wang et al., A review of THz modulators with dynamic tunable metasurfaces. Nanomaterials. 9(7), 965 (2019)

12. J. Qin et al., Metasurface Micro/Nano-Optical Sensors: Principles and Applications. ACS Nano. 16(8), 11598–11618 (2022)

13. S. Chang, X. Guo, X. Ni, Optical Metasurfaces: Progress and Applications. Annual Rev Mater Res 48(48), 279–302 (2018)

14. A.E. Minovich et al., Functional and nonlinear optical metasurfaces. Laser Photonics Rev. 9(2), 195–213 (2015)

15. M.R. Tavakol, B. Rahmani, A. Khavasi, Tunable polarization converter based on one-dimensional graphene metasurfaces. J. Opt. Soc. Am. B 35(10), 2574–2581 (2018)

16. L. La Spada, Metasurfaces for advanced sensing and diagnostics. Sensors 19, 355 (2019). https:/ /doi.or g/10.33 90/s1 9020355

17. J. Zhang et al., Bi-functional switchable broadband terahertz polarization converter based on a hybrid graphene-metal meta surface. Opt. Express. 28(18), 26102–26110 (2020)

18. Y. Zhang et al., Graphene-Based Tunable Polarization Conversion Metasurface for Array Antenna Radar Cross-Section Reduction. Sensors. 24(15), 5044 (2024)

19. M. Amin et al., A THz graphene metasurface for polarization selective virus sensing. Carbon. 176, 580–591 (2021)

20. F. Ding, A. Pors, S.I. Bozhevolnyi, Gradient metasurfaces: a review of fundamentals and applications. Rep. Prog. Phys. 81(2), 026401 (2018)

21. Q. He et al., High-efficiency metasurfaces: principles, realizations, and applications. Adv. Opt. Mater. 6(19), 1800415 (2018)

22. C. Li, Q. Wu, Graphene-based tunable high-sensitivity metasurface refractive index sensor. Plasmonics 20(2), 951–962 (2025)

23. B. Lv et al., Ultra-wideband and angular-stable terahertz reflective cross-polarization converter integrated with highly sensitive biosensing. Mater. Res. Bull. 193, 113641 (2026)

24. S. Ponlatha et al., Next-generation hybrid multi-material surface plasmon resonance biosensor for non-invasive glucose detection with machine learning optimization. Plasmonics 20(12), 11119-11135 (2025)

25. U. Arun Kumar et al., MXene-BP-graphene metasurface terahertz biosensor for high-sensitivity detection of carcinoembryonic antigen and malaria histidine-rich protein II. Microsyst. Technol. 31(12), 4037–4056 (2025)

26. N. Vithyalakshmi et al., High-Performance Dual-Mode Terahertz Biosensor for Cancer Detection via Graphene Modulation and Machine Learning Integration. Sens. Imaging. 26(1), 146 (2025)

27. T. Sheheryar et al., Multispectral terahertz metasurface biosensor supporting multi-disease identification and chemical sensing. Opt. Quant. Electron. 58(1), 44 (2025)

28. T. Sheheryar, X. Dong, X. Wang, B. Lv, “High-Efficiency Graphene-Based Terahertz Polarization Converter with Integrated Biological Sensing and Tunable Performance,” *ACS Applied Optical Materials*, 3(10), 2384–2398 (2025).

29. B. Lv, S. Wang, P. Wang, T. Sheheryar, H. Tao, “Graphene-integrated ultra-broadband terahertz polarization converter for high-sensitivity bio-chemical sensing,” *Diamond and Related Materials* (2026).

30. T. Sheheryar, B. Lv, X. Wang, X. Dong, L. Gao, B. Xie, “Ultra-wideband graphene-assisted Terahertz Sensor with tunable polarization conversion for chemical sensing,” *Materials Research Bulletin*, 195, 113806 (2026).

31. N. Ben Ali, V. Dhasarathan, T. Sheheryar, Y. M. Al-Moliki, “Terahertz polarization-converting graphene metasurface with integrated biosensing and chemical sensing for multi-analyte detection,” *Measurement*, 263, 120190 (2026).

32. K.-T. Lin et al., Structured graphene metamaterial selective absorbers for high efficiency and omnidirectional solar thermal energy conversion. Nat. Commun. 11(1), 1389 (2020)

33. J. Zhang et al., Towards photodetection with high efficiency and tunable spectral selectivity: graphene plasmonics for light trapping and absorption engineering. Nanoscale. 7(32), 13530–13536 (2015)

34. H. Hu et al., A graphene-based THz metasurface sensor with air-spaced structure. Front. Phys. 10, 990126 (2022)

35. E. Veisi et al., Highly sensitive multi-mode tunable THz graphene-based refractive index biosensor. Results Opt. (2025). https: //doi. or g/10. 10 1 6/j. rio. 2025.100948

36. Y.Z. Cheng et al., Ultrabroadband reflective polarization converter for terahertz waves. Appl. Phys. Lett. 105(18), 181111 (2014)

37. R.T. Ako et al., Ultra-wideband tri-layer transmissive linear polarization converter for terahertz waves. APL Photonics. 5(4), 046101 (2020)

38. R.T. Ako et al., Broadband and wide-angle reflective linear polarization converter for terahertz waves. APL Photonics. 4(9), 096104 (2019)

39. T. Sheheryar et al., Ultra-wideband reflecting linear cross-polarization converter with integrated high-sensitivity biosensing. Opt. Quant. Electron. 57(8), 427 (2025)

40. V. Maurya, S. Singhal, Ultrathin reflecting wideband terahertz cross-polarization converter as a biosensor. Mater. Res. Bull. 185, 113292 (2025)

41. Nelson, I., and C. Annadurai. "Tunable metasurface for broadband polarization conversion and high-sensitivity biosensing through graphene conductivity control." *Applied Physics A* 132 (2026): 796.

42. S.K. Patel, J. Surve, J. Parmar, Detection of cancer with graphene metasurface-based highly efficient sensors. Diamond Relat. Mater. 129, 109367 (2022)

43. T. Parvin et al., Differential optical absorption spectroscopy-based refractive index sensor for cancer cell detection. Opt. Rev. 28, 134–143 (2021)

44. S. Banerjee et al., A theoretical terahertz metamaterial absorber structure with a high-quality factor using two circular ring resonators for biomedical sensing. Inventions. 6(4), 78 (2021)

45. R. Khan et al., Refractive index of biological tissues: review, measurement techniques, and applications. Photodiagn. Photo dyn. Ther. 33, 102192 (2021)

46. P. Upender, A. Kumar, Ultrathin, ultra-narrow band DMMA for biosensing applications. IEEE Trans. Nanobioscience 22(3), 529 537 (2022)

47. X. Huang, B. Wang, High-sensitivity terahertz sensor based on semiconductor material for biosensing detection. J. Mater. Chem. C 13(10), 5148–5160 (2025)

48. V. Maurya, S. Singhal, Ultrathin Multiband Polarization-Independent Terahertz Absorber as

a Biosensor. IEEE Sens. J. 23(21), 25919–25926 (2023)

49. H.R. Seren et al., Optically modulated multiband terahertz perfect absorber. Adv. Opt. Mater. 2(12), 1221–1226 (2014)

50. H.-T. Chen et al., Active terahertz metamaterial devices. Nature. 444(7119), 597–600 (2006)

51. H. Tao et al., " Highly flexible wide-angle of incidence terahertz metamaterial absorber: Design, fabrication, and characterization. Phys. Rev. B 78(24), 241103 (2008)

52. N.-H. Shen et al., optically implemented broadband blueshift switch in the terahertz regime. Phys. Rev. Lett. 106(3), 037403 (2011)

53. X. Liu et al., Laser etching of aluminum thin film on polyimide: Simulation and experimental studies. Surf. Coat. Technol. 277, 107–116 (2015)

54. S. Hadipour, P. Rezaei, A. Norouzi-Razani, Multi-band square-shaped polarization-insensitive graphene-based perfect absorber. Opt. Quant. Electron. 56(3), 471 (2024)

55. X. Qin et al., Design of terahertz metamaterial absorbers with switchable absorption functions utilizing thermal and electrical dual-modulation strategies. Nanoscale. 16(34), 16238–16250 (2024)

56. R. Zheng et al., Ultra-wideband tunable terahertz metamaterial absorber based on single-layer graphene strip. Diamond Relat. Mater. 141, 110713 (2024)

57. S. Barzegar-Parizi, A. Ebrahimi, K. Ghorbani, Two-bit dual-band switchable terahertz absorber enabled by composite graphene and vanadium dioxide metamaterials. Sci. Rep. 14(1), 5818 (2024)

58. T. Chen et al., Design of a terahertz metamaterial sensor based on a split-ring resonator nested square ring resonator. Mater. Res. Express. 7(9), 095802 (2020)

59. L. Zhu et al., Dual-band electromagnetically induced transparency (EIT) terahertz metamaterial sensor. Opt. Mater. Express. 11(7), 2109–2121 (2021)

60. G. Deng et al., A Metamaterial-Based Absorber for Liquid Sensing in the Terahertz Regime. IEEE Sens. J. 22(22), 21659–21665 (2022)

61. S. Anwar, M. Khan, High-performance terahertz refractive index sensor for cancer cells detection. Eur. Phys. J. E. 46(3), 19 (2023)

62. V. Maurya, S. Singhal, Dual Band Terahertz Reflective Linear Cross Polarization Converter-Based Biosensor. IEEE Sens. J. 24(5), 6103–6110 (2024)

63. T. Sheheryar et al., An ultra-wideband terahertz linear cross-polarization converter with integrated biosensing for multi-disease diagnosis. J. Mater. Chem. C 13(24), 12460–12471 (2025)